

Effect of rolling deformation on the microstructure of bulk $\text{Cu}_{60}\text{Zr}_{20}\text{Ti}_{20}$ metallic glass and its crystallization

Q.P. Cao ^a, J.F. Li ^{a,*}, Y.H. Zhou ^a, A. Horsewell ^b, J.Z. Jiang ^{c,*}

^a State Key Laboratory of Metal Matrix Composites, School of Materials Science and Engineering, Shanghai Jiao Tong University, 1954 Huashan Road, Shanghai 200030, People's Republic of China

^b Department of Manufacturing Engineering and Management, Building 204, Technical University of Denmark, DK-2800 Lyngby, Denmark

^c Laboratory of New-Structured Materials, Department of Materials Science and Engineering, Zhejiang University, Hangzhou 310027, People's Republic of China

Received 23 December 2005; received in revised form 22 May 2006; accepted 22 May 2006
Available online 9 August 2006

Abstract

Bulk $\text{Cu}_{60}\text{Zr}_{20}\text{Ti}_{20}$ metallic glass has been rolled at room temperature (RT) and cryogenic temperature (CT) up to 97% in thickness reduction, and the dependences of microstructure on the strain and temperature have been investigated. It is revealed that as the deformation proceeds below a critical thickness reduction, which is 87% at RT and 89% at CT, only the shear band density and the free-volume content increase, whereas the thermal stability of the deformed glass remains unchanged. Deformation above the critical thickness reduction results in phase separation plus nanocrystallization at RT, but only phase separation at CT, indicating that lowering the temperature can effectively retard the deformation-driven crystallization, and that phase separation is the precursor of crystallization. The appearances of phase separation and especially nanocrystallization reduce the thermal stability of the glass since they create advantages in chemical composition and topological structure for the primary crystalline phase to nucleate and grow.

© 2006 Acta Materialia Inc. Published by Elsevier Ltd. All rights reserved.

Keywords: Metallic glass; Plastic deformation; Phase separation; Crystallization; Free volume

1. Introduction

Metallic glasses possess high strength, hardness and elastic deformation limit [1–3]. However, during compressive or tensile testing at temperatures far below the glass transition temperature, they often break abruptly along a very narrow shear band, and exhibit little global plasticity [4]. Such a catastrophic fracture greatly limits the application of metallic glasses as structural materials, and much attention has been focused on the fracture mechanism [5–9].

By examining broken samples, it has been clearly revealed that glass fracture is accompanied by a partial crystallization, indicated by the nanocrystalline precipita-

tion around the fracture zones [10]. Considering that liquid droplets sometimes exist on the fracture surface, some researchers speculated that the material near the fracture could be adiabatically heated above the melting point when cracks rapidly propagate in the glasses [4,11,12], and such a temperature rise caused crystallization. However, when an $\text{Al}_{90}\text{Fe}_5\text{Gd}_5$ metallic glass ribbon underwent a repeated bending deformation at 233 K but did not fracture, nanocrystallization was still observed [13]. Since the deformation heat could be easily dissipated and the temperature rise in the sample was very limited in such a subambient case, deformation-induced crystallization was therefore advanced. This argument was further supported by nanoin-dentation experiments on metallic glasses [14,15]. Without a significant heating effect, the deformed glass around the nanoindenter was crystallized. These results mean that crystallization can be triggered not only by a heating effect but also by mechanical deformation.

* Corresponding authors. Tel.: +86 21 6293 3785; fax: +86 21 6293 2026.
E-mail addresses: jfli@sjtu.edu.cn (J.F. Li), jiangjz@zju.edu.cn (J.Z. Jiang).

To understand the mechanical behaviors of metallic glasses, it is necessary to investigate the microstructure evolution of metallic glasses with plastic deformation. In addition, mechanical deformation is also a potential alternative route for fabricating nanocrystals/glass composites [16]. Compared with the nanocrystals/glass materials prepared by directly casting or annealing the glasses, this type of composite contains more free volume and different short-range orders in the glass matrix [17,18], and it is hoped this process will play an important role in improving the mechanical properties [19,20]. It is certain that we also need to know the stability against heating.

Because of the poor ductility, plastic deformation of metallic glasses at temperatures far below their glass transition temperatures can only be achieved by the compressive method at low strain rates. However, the deformation degree achieved in conventional metallic glasses is considerably limited by their small thickness, and as a result the detailed relationship between the microstructure of metallic glasses and plastic strain is still far from being understood. The discovery of bulk metallic glasses (BMGs) has made it possible to resolve this problem [2]. In the work reported in the present paper we rolled a $\text{Cu}_{60}\text{Zr}_{20}\text{Ti}_{20}$ BMG to a higher strain level both at room temperature (RT) and cryogenic temperature (CT) so as to investigate the microstructure evolution. The decrease in rolling temperature is expected to be helpful for revealing the activation behavior of atoms driven by mechanical force.

2. Experimental

Ternary $\text{Cu}_{60}\text{Zr}_{20}\text{Ti}_{20}$ (in at.%) alloy was chosen as the experimental material mainly because of its good ductility in the glassy state and possible application in engineering materials due to its high strength and low cost. A master alloy ingot with nominal composition $\text{Cu}_{60}\text{Zr}_{20}\text{Ti}_{20}$ was prepared by arc melting high-purity Cu (99.99%), Zr (99.9%) and Ti (99.9%) under a Ti-gettered argon atmosphere. The ingot was inverted and remelted six times to ensure its microstructural homogeneity and then suck-cast into a water-cooled Cu mold to produce a 40 mm long cylindrical rod with a diameter of 2 mm. The amorphous structure was ascertained by X-ray diffraction (XRD) and high-resolution transmission electron microscopy (HRTEM). The rods were cut into short cylinders with a thickness of 1.5 mm for rolling. Both ends of the cylinders were mechanically polished to make them parallel to each other prior to the rolling experiment. During the CT rolling deformation, a continuous liquid nitrogen stream was used to cool the specimen, and the temperature of the specimen was measured to be about 150 K using a type-K thermocouple. For comparison, another set of specimens was rolled at RT. The rolling apparatus consisted of two 100 mm diameter rollers. Covered by two steel plates with 1 mm original thickness, the specimen was repeatedly rolled in one direction until the desired deformation was

obtained. The deformation degree is denoted by the reduction in thickness $\varepsilon = (h_0 - h)/h_0$, where h_0 and h represent the specimen thicknesses before and after rolling, respectively. Many small deformation passes were used with a progressively narrowing gap between the two rollers. The decrease of the gap during rolling was carefully controlled so that the strain rate was about $5.0 \times 10^{-3} \text{ s}^{-1}$.

The microstructures of the specimens subjected to different degrees of deformation were examined using a Philips PW1820 X-ray diffractometer with monochromatic Cu K_α radiation and a JEOL JEM-3000 F HRTEM instrument operating at 300 kV. To prevent contamination and crystallization caused by electrochemical twin-jet polishing and ion milling at RT [21], the thin foil specimens for TEM were prepared by low-energy ion milling at 2.5 keV and 5 mA with liquid nitrogen cooling. The specimens were observed using TEM immediately after the preparation since the Cu–Zr–Ti thin foil readily oxidizes upon exposure in air atmosphere. Selected area electron diffraction (SAED) patterns were obtained from an area about 0.1 μm in diameter. Local chemical composition was determined by energy dispersive X-ray (EDX) analysis. Thermal analysis was performed using a Perkin–Elmer Pyris Diamond differential scanning calorimetry (DSC) instrument at heating rates from 10 to 80 K/min under a flow of purified argon. A second run under identical conditions was used to determine the baseline after each measurement run. The sample and reference pans were made of Al. The temperature and the heat flow were calibrated by measuring the melting temperatures and the heats of fusion of pure In, Sn and Zn.

3. Results

3.1. XRD patterns

The XRD pattern of the as-cast $\text{Cu}_{60}\text{Zr}_{20}\text{Ti}_{20}$ specimen is shown in Fig. 1. Besides two broad diffraction peaks, no signals from crystalline phases were detected. As the $\text{Cu}_{60}\text{Zr}_{20}\text{Ti}_{20}$ alloy comprising amorphous matrix and

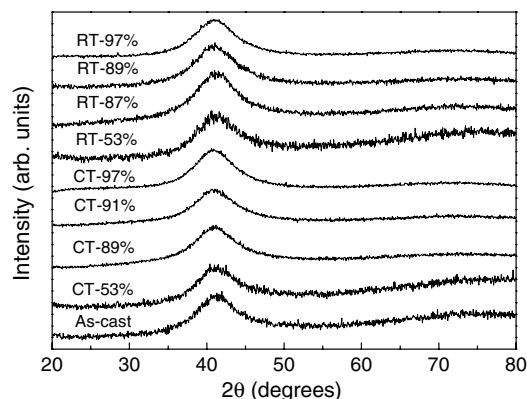


Fig. 1. XRD patterns for the as-rolled $\text{Cu}_{60}\text{Zr}_{20}\text{Ti}_{20}$ specimens with different ε . The data for CT-rolled specimens are taken from Ref. [20].

primary nanocrystalline phase also exhibits amorphous-like diffraction characteristic in the XRD pattern [22]. TEM analyses of the as-cast specimen were conducted to ascertain that they were amorphous in nature. Fig. 2a shows the bright-field image, and a uniform featureless contrast was observed. The inset shows a corresponding SAED pattern. It consists of a broad diffraction halo and a faint larger one, which are typical for amorphous materials. Additionally, the microstructure of the as-cast specimen was observed using HRTEM, and no lattice fringes were found (Fig. 2b). Therefore, we can confirm that the as-cast $\text{Cu}_{60}\text{Zr}_{20}\text{Ti}_{20}$ alloy rod of 2 mm in diameter is completely amorphous.

The maximum thickness reductions achieved at RT and CT are both 97%. The specimens with such a high ϵ remained ductile, as shown by a 180° bending without fracture. Fig. 3 shows the outer images of the RT-rolled specimens with $\epsilon = 0\%$, 53% and 97%, and the image of the 180° bent specimen with $\epsilon = 97\%$ is shown in the inset.

Although no crystalline phases were detected by XRD in the RT-rolled and CT-rolled $\text{Cu}_{60}\text{Zr}_{20}\text{Ti}_{20}$ specimens with each ϵ , as shown in Fig. 1, fitting the broad diffraction peak located at $2\theta \approx 41^\circ$ using a Gauss line profile indicated a variation of the full width at the half maximum (FWHM) with ϵ , as shown in Fig. 4. It is clear that the FWHM increases by about 3% from the as-cast specimen to the RT-rolled specimen with $\epsilon = 87\%$ and then decreases by about 4% from $\epsilon = 87\%$ to 97% . For the CT-rolled specimens, the FWHM increases by about 9% as ϵ changes from 0% to 89%, and then decreases by about 3% when ϵ varies from 89% to 97%. Obviously, the rolling deformation at CT results in a slightly larger FWHM value and shifts the peak value of FWHM to a higher thickness reduction ϵ as compared with the rolling deformation at RT.

3.2. DSC curves

Fig. 5a and b depicts the typical DSC curves of the RT-rolled and CT-rolled specimens with different ϵ at a heating rate of 20 K/min. The as-cast alloy exhibits an endothermic

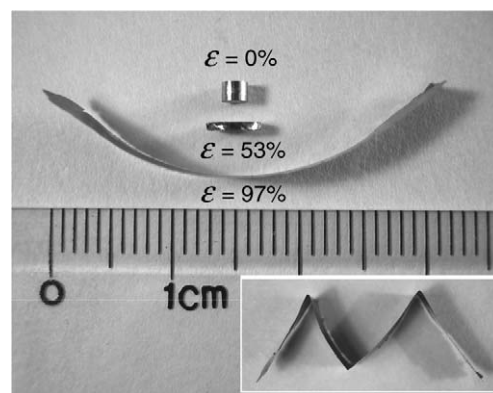


Fig. 3. Image of the RT-rolled specimen with $\epsilon = 0\%$, 53% and 97%. The inset is the shape of the specimen with $\epsilon = 97\%$ having undergone a 180° bend.

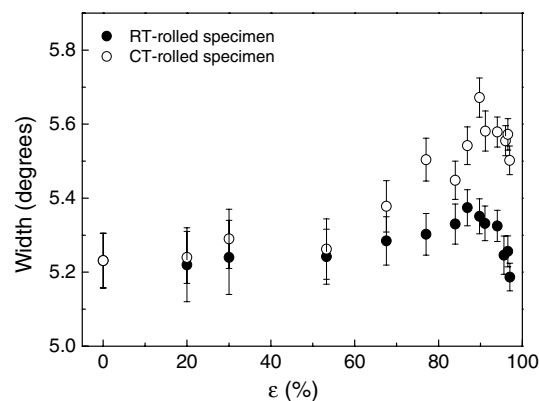


Fig. 4. FWHM of XRD peaks of the as-rolled specimens. The diffraction peaks were fitted by the Gauss line profile.

event, characterized by a glass transition temperature $T_g = 706$ K, followed by two exothermic events, characterized by the onset temperature for crystallization $T_x = 736$ K, the peak temperature for the first crystallization event $T_{p1} = 748$ K and the peak temperature for the second crystallization event $T_{p2} = 786$ K. The first exothermic event corresponds to the amorphous-to- $\text{Cu}_{51}\text{Zr}_{14}$

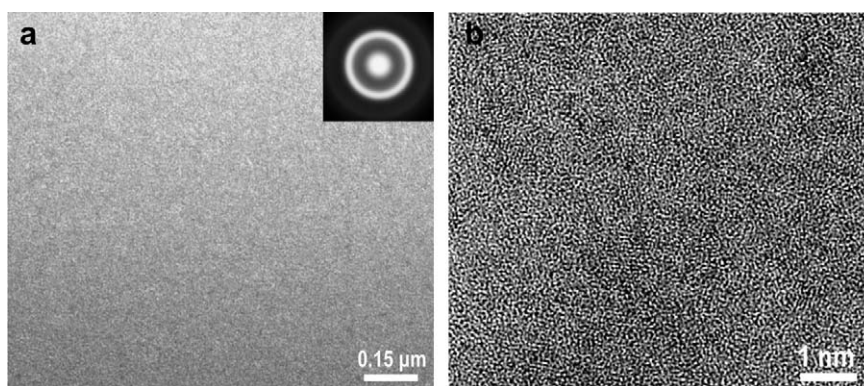


Fig. 2. TEM (a) and HRTEM (b) bright-field images of the as-cast $\text{Cu}_{60}\text{Zr}_{20}\text{Ti}_{20}$ specimen. The inset in (a) is a SAED pattern.

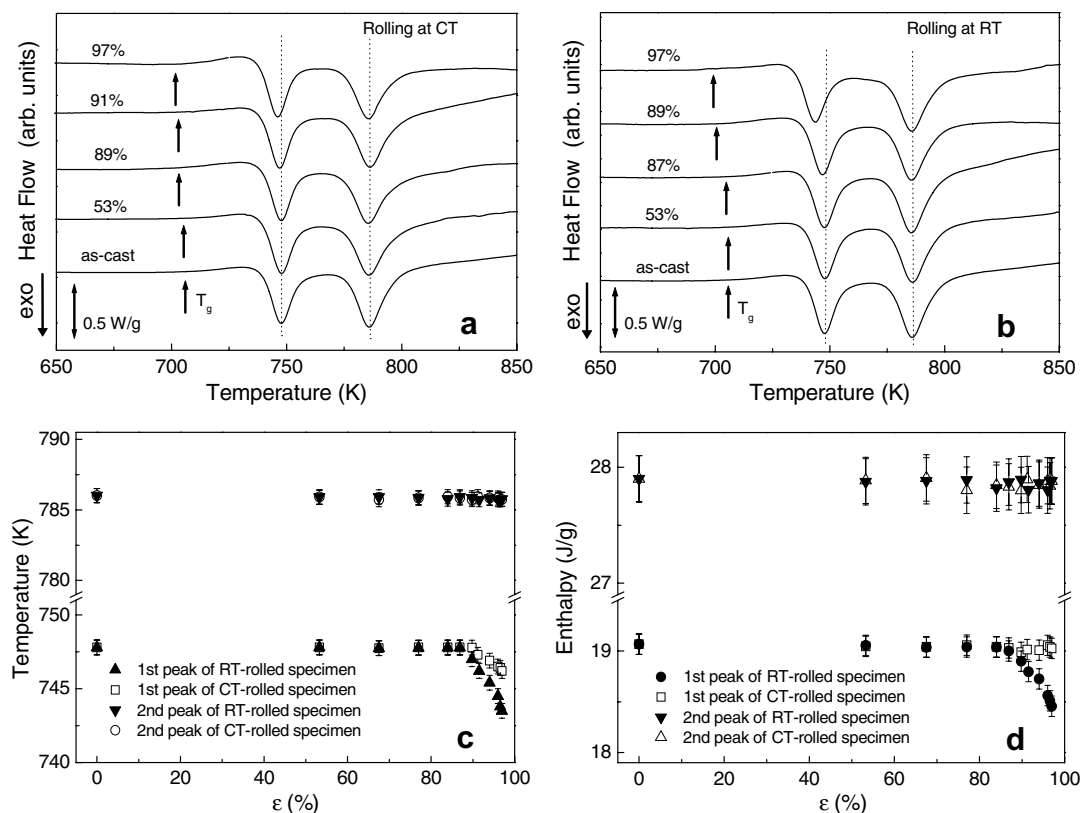


Fig. 5. DSC curves of the CT-rolled (a) and RT-rolled (b) specimens with different ϵ at a heating rate of 20 K/min. The peak temperatures and enthalpies of the first and second exothermic events as a function of ϵ are plotted in (c) and (d). Some of the data of (a), (b) and (d) are taken from Ref. [20].

phase transition while the second one is due to the crystallization of the residual amorphous phase [23,24]. Strain dependences of the first and second peak temperatures and enthalpies for the RT-rolled and CT-rolled specimens are shown in Fig. 5c and d, respectively. In the initial stage of rolling deformation, the first peak temperature remains unchanged for the RT-rolled specimens with $\epsilon \leq 87\%$ and the CT-rolled specimens with $\epsilon \leq 89\%$. Upon further increasing ϵ , the first peak temperature decreases by 4 K from $\epsilon = 87\%$ to 97% for the RT-rolled specimens, while for the CT-rolled specimens it only decreases by 1.5 K as ϵ changes from 89% to 97%. The second peak temperatures for the RT-rolled and CT-rolled specimens do not vary with ϵ during the whole deformation process. It is clearly seen that compared with the rolling deformation at CT, the RT rolling leads to a larger decrease of the thermal stability of the alloy when ϵ exceeds the critical value. For the enthalpy of the first exothermic event, the measurement results indicate that it remains invariable for the RT-rolled specimens with $\epsilon \leq 87\%$, but then decreases by about 3% from $\epsilon = 87\%$ to 97%, while that for the CT-rolled specimens remains unchanged at all ϵ values. The enthalpy of the second exothermic event does not change with ϵ whether the rolling is performed at RT or CT. Such results indicate that crystallization is involved in the RT-rolled specimens with $\epsilon > 87\%$, while the possibility of crystallization in the CT-rolled specimens can be excluded.

3.3. Microstructure evolution during rolling

3.3.1. TEM images of the CT-rolled specimens

Since the enthalpy of the first exothermic event for the specimen rolled at CT does not vary with ϵ during the whole rolling deformation, whereas the first peak temperature gradually decreases as $\epsilon > 89\%$, we were motivated to probe possible microstructural changes in the as-rolled specimens. As deformation of metallic glasses at low temperatures and high stresses is inhomogeneous [25], the softening induced by the increasing free-volume content permits localized strain and the deformation is confined to the narrow regions near the shear bands [26]. These regions, therefore, are more favorable for deformation-induced microstructural changes than the regions far away from the shear bands. Fig. 6a shows a bright-field TEM image of the CT-rolled specimen with $\epsilon = 89\%$. Similar to the TEM images of other CT-rolled specimens for $\epsilon < 89\%$, no strong contrast was observed except for an increase in the density of shear bands. The insets in Fig. 6a are the SAED patterns taken from a shear band and an area far from the shear bands, and each of them consists of two broad diffraction haloes, indicating the amorphous nature of the structure. The SAED pattern from the area far from the shear bands is very similar to that from the as-cast specimen, while the width of the first diffraction halo of the SAED pattern from the shear band

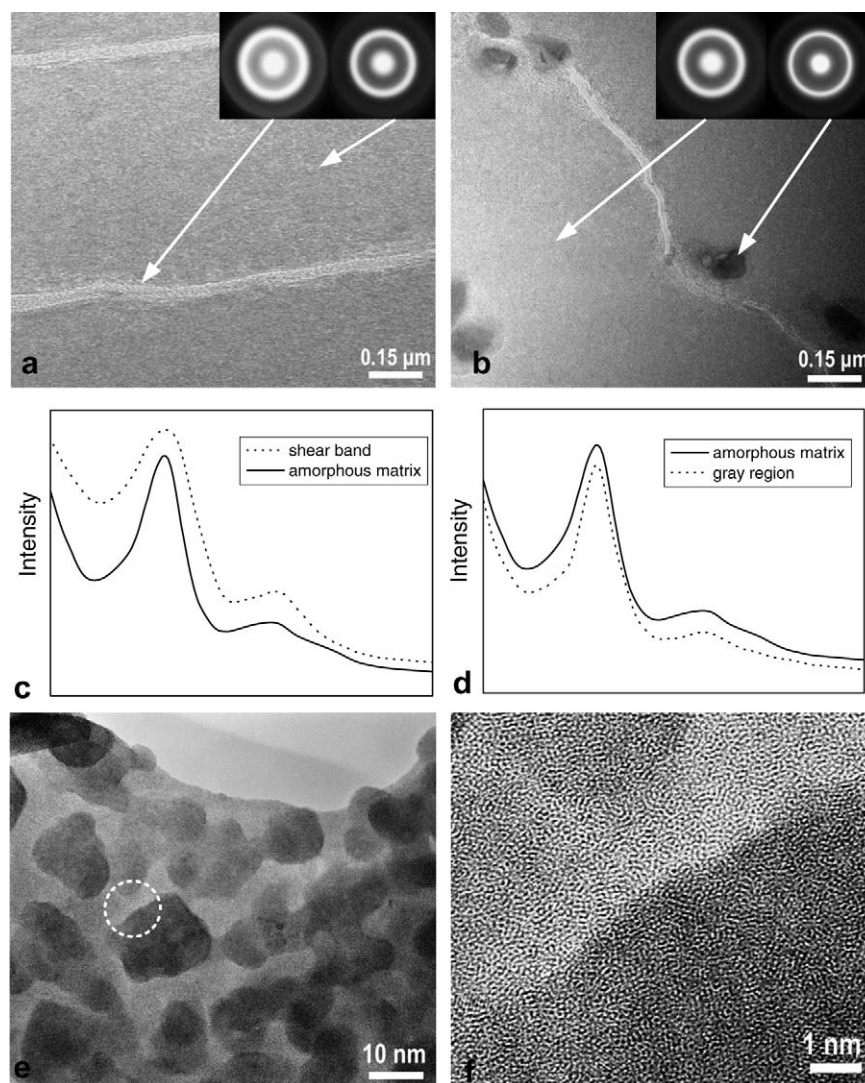


Fig. 6. TEM images of the CT-rolled specimens with $\varepsilon = 89\%$ (a) and $\varepsilon = 97\%$ (b). The insets are the SAED patterns from the marked areas. (c, d) Intensity profiles of the SAED patterns in (a) and (b). (e) Magnified TEM image of the gray region in (b). (f) HRTEM image of the selected area in (e). The TEM images are taken from Ref. [20].

increases considerably compared with that from the as-cast specimen. As ε exceeds 89%, some gray regions near the shear bands begin to appear in the microstructure and their number and size increase with ε . A TEM image of the specimen deformed by $\varepsilon = 97\%$ is shown in Fig. 6b, where the sizes of the gray regions are in the range 100–120 nm. The SAED patterns obtained from the gray region and the amorphous matrix are shown in the inset, and only diffraction haloes are observed. Compared with the SAED pattern from the as-cast amorphous alloy in Fig. 2a, the width of the first diffraction halo from the matrix of the amorphous alloy in Fig. 6b also remains invariable, while that from the gray region decreases significantly. As the exposure time for obtaining the SAED patterns was fixed, the variation of the width of the halo of the SAED pattern should reflect the difference in microstructure. In order to confirm this argument, the intensity profiles of the SAED patterns in Fig. 6a and b are shown in Fig. 6c and d, respec-

tively. It is clear that the FWHM of the first diffraction halo of the SAED pattern from the shear band increases considerably due to the deformation-enhanced atomic disorder, i.e. the increased free-volume content, as compared with that from the amorphous matrix. Meanwhile, the FWHM from the gray region decreases significantly. This observation is consistent with the free-volume model, which predicts that after the localized deformation event, the free-volume content within the shear band should be greater than that in the undeformed material, increasing the average free-volume content [27].

It should be mentioned that the gray regions are uneven in structure at higher magnification. A TEM image of the specimen with $\varepsilon = 97\%$ is shown in Fig. 6e, where the microstructure consists of a brighter matrix and darker substructures with an average size of about 10–20 nm. Their chemical compositions were estimated by nanobeam EDX with a beam size of about 3 nm and the results are

summarized in Table 1. The average composition in the darker substructures is 70.0 at.% Cu, 13.3 at.% Ti and 16.7 at.% Zr, while the brighter matrix contains 54.3 at.% Cu, 20.7 at.% Ti and 25.0 at.% Zr. Fig. 6f shows the HRTEM image of the selected area in Fig. 6e. No lattice fringes are observed in the darker substructure and the brighter matrix. Hence, it is clear that the distinction in contrast among the different regions results from the composition fluctuation, and a mechanically driven phase separation rather than crystallization occurs in the CT-rolled specimens when ε exceeds 89%.

3.3.2. TEM images of the RT-rolled specimens

Fig. 7a shows a bright-field TEM image of the RT-rolled specimen with $\varepsilon = 87\%$. Similar to Fig. 6a, no obvious contrast was observed except for the shear band. The SAED patterns from the shear band and the area far away from the shear band, as shown in the insets, consist of a broad diffraction halo and a faint larger one, characteristic of a glassy structure. As ε exceeds 87%, some gray regions near shear bands begin to appear in the microstructure and their number and size increase with ε . A TEM image of the specimen deformed by $\varepsilon = 97\%$ is shown in Fig. 7b, where the sizes of the gray regions are in the range 90–130 nm. The SAED patterns obtained from the gray region and the amorphous matrix are shown in the inset, and only diffraction haloes are observed. The intensity profiles of the SAED patterns in Fig. 7a and b are shown in Fig. 7c and d, respectively. It is clear in Fig. 7c that the FWHM of the first diffraction halo of the SAED pattern from the shear band is considerably larger than that from the amorphous matrix, but evidently less than that from the CT-rolled shear band (Fig. 6c). In Fig. 7d, the FWHM of the first diffraction halo from the gray region is not only less than that from the amorphous matrix, but also less than that from the CT-rolled gray region (Fig. 6d).

A TEM image of the gray regions in the specimen with $\varepsilon = 97\%$ at higher magnification is shown in Fig. 7e. The microstructure also consists of a brighter matrix and darker substructures with an average size of about 8–20 nm. Fig. 7f–h shows the HRTEM images of the selected areas

in Fig. 7e. No obvious lattice fringes are observed in the brighter matrix and darker area marked by I and II, respectively. However, precipitated nanocrystals are found in the darker area marked by III, confirmed by the evident lattice fringes in the HRTEM image. Chemical compositions of the brighter matrix, the darker amorphous structures and precipitated nanocrystals were estimated by EDX with a beam size of about 3 nm and the results are summarized in Table 1. The average composition in the darker amorphous substructures is 73.3 at.% Cu, 11.1 at.% Ti and 15.6 at.% Zr, and the brighter matrix contains 50.2 at.% Cu, 22.7 at.% Ti and 27.1 at.% Zr, while the average composition in nanocrystals is 78.1 at.% Cu, 7.0 at.% Ti and 14.9 at.% Zr. The Cu concentration in the matrix, darker amorphous structures and nanocrystals increases sequentially. Hence, it is clear that mechanically driven phase separation and nanocrystallization have occurred in the RT-rolled specimens when ε exceeds 87%, and phase separation is the precursor of crystallization.

3.4. Crystallization kinetics

To further investigate the effect of rolling on the thermal stability of $\text{Cu}_{60}\text{Zr}_{20}\text{Ti}_{20}$ specimen, a series of isochronal DSC measurements were performed on the specimens that had been annealed isothermally for various times at 708 K, a temperature slightly higher than the glass transition temperature. Fig. 8a–c shows the DSC curves of the as-cast specimen, the RT-rolled and CT-rolled specimens with $\varepsilon = 97\%$, respectively. The isothermal annealing at 708 K only promotes the precipitation of the primary phase, but will not lead to the precipitation of the phase involved in the second exothermic peak on the DSC curves, when the holding time is not too long. The time dependence of the enthalpy of the first exothermic event for these three kinds of specimen is shown in Fig. 7d. Upon increasing the annealing time, the enthalpy for the as-cast specimen decreases from 19 J/g to close to 0 J/g when the annealing time increases from 0 to 90 min. For the RT- and CT-rolled specimens, annealing at 708 K for 40 and 60 min, respectively, is enough for them to complete the first exothermic event. Obviously, crystallization of the primary phase during the isothermal annealing at 708 K is the most rapid for the RT-rolled specimen, but the slowest for the as-cast specimen. In contrast, the enthalpy of the second exothermic event for the RT-rolled and CT-rolled specimens with $\varepsilon = 97\%$ is independent of the isothermal annealing process, and is the same as that of the as-cast specimen. These experimental results further confirm that the RT-rolled specimen with $\varepsilon = 97\%$ has the lowest thermal stability against crystallization.

The crystallization activation energy is an important kinetic parameter reflecting the thermal stability of amorphous alloys as well as the local atomic structure [28]. DSC measurements performed at different heating rates were used to determine the activation energy for the

Table 1
Composition distributions in the rolled $\text{Cu}_{60}\text{Zr}_{20}\text{Ti}_{20}$ specimens with $\varepsilon = 97\%$

Specimen	Area	Cu (at.%)	Zr (at.%)	Ti (at.%)
CT-rolled	A	60.3 ± 1.0	19.9 ± 0.5	19.8 ± 0.6
	B	54.3 ± 3.1	25.0 ± 2.0	20.7 ± 1.6
	C	70.0 ± 2.5	16.7 ± 2.0	13.3 ± 1.2
RT-rolled	D	60.6 ± 1.8	19.4 ± 1.0	20.0 ± 0.8
	E	50.2 ± 3.0	27.1 ± 1.4	22.7 ± 2.0
	F	73.3 ± 2.3	15.6 ± 1.1	11.1 ± 1.0
	G	78.1 ± 3.1	14.9 ± 1.7	7.0 ± 0.6

A and D represent an arbitrary area with a size of $1 \mu\text{m}^2$ in the measured specimens. B and E denote the brighter matrices in the gray regions, C and F the darker amorphous substructures in the gray regions, and G the precipitated nanocrystals.

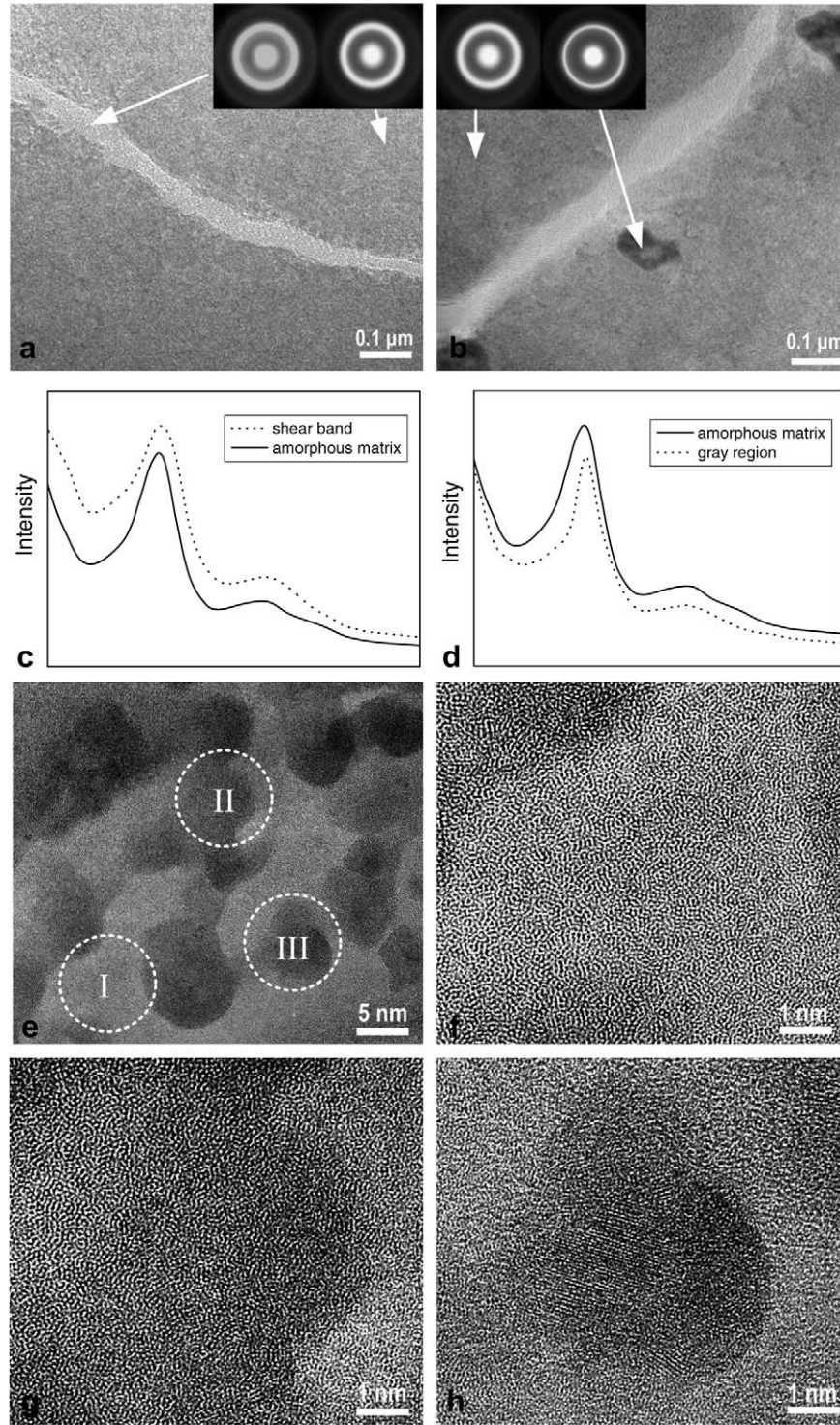


Fig. 7. TEM images of the RT-rolled specimens with $\varepsilon = 87\%$ (a) and $\varepsilon = 97\%$ (b). The insets are the SAED patterns of the marked regions. (c, d) Intensity profiles of the SAED patterns in (a) and (b). (e) Magnified TEM image of the gray region in (b). (f–h) HRTEM images of the selected areas marked I, II and III in (e), respectively. Note that a lattice fringe has appeared in (h), while the darker substructure in (g) is still amorphous.

nucleation and growth. Fig. 9a–c shows the typical DSC curves at heating rates of 10, 20, 40 and 80 K/min. T_g , T_x , T_{p1} and T_{p2} are shifted to higher temperature with increasing the heating rate. The effective activation energy for crystallization can be evaluated by Kissinger's equation [29] as follows:

$$\ln(\phi/T_{pi}^2) = -E_i/RT_{pi} + C_i \quad (1)$$

where ϕ is the heating rate, T_{pi} is the peak temperature for crystallization reaction i ($i = 1$ represents the first crystallization process; $i = 2$ the second one), E_i is the corresponding effective activation energy, R is the gas constant and C_i

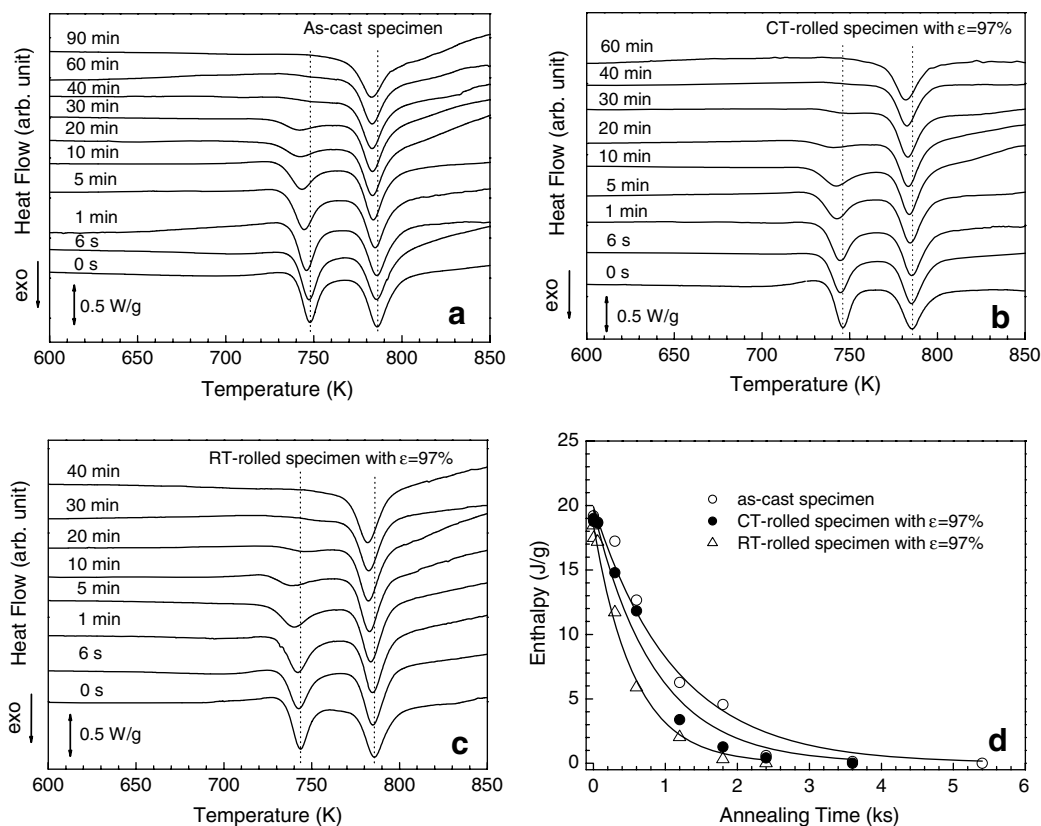


Fig. 8. DSC curves of the as-cast specimen (a) and the CT-rolled (b) and RT-rolled (c) specimens with $\varepsilon = 97\%$ after annealing at 708 K for various times. The heating rate is 20 K/min. (d) The time dependence of the enthalpy of the first exothermic event for the three specimens. Solid lines are for guidance.

is a constant for the reaction. Fig. 9d shows the Kissinger plots of $\ln(\phi/T_{pi}^2)$ versus $1/T_{pi}$ for the two crystallization events for the as-cast specimen and the CT- and RT-rolled specimens with $\varepsilon = 97\%$. The effective activation energies derived from the slope of the Kissinger plots for the second crystallization event, E_2 , are 307 ± 12 , 302 ± 11 and 301 ± 11 kJ/mol, respectively. They are the same within experimental error, also indicating that any microstructural changes during rolling have no influence on the second crystallization event. The effective activation energy, E_1 , for the formation of primary $\text{Cu}_{51}\text{Zr}_{14}$ phase in the as-cast specimen is 372 ± 17 kJ/mol, which is in good agreement with the value obtained by Concustell et al. [23]. As the specimen is rolled at CT up to $\varepsilon = 97\%$, E_1 decreases to 353 ± 14 kJ/mol. The value of E_1 is further decreased to 336 ± 18 kJ/mol when the specimen is rolled at RT up to $\varepsilon = 97\%$. This clearly indicates that E_1 is markedly influenced by the microstructural change induced by rolling deformation.

4. Discussion

4.1. Microstructure evolution induced by deformation

Different from crystalline materials, metallic glasses lack the long-range regular arrangement in the atomic assembly. Their plastic deformation is realized by a number of

individual atomic jumps rather than the multiplication and slide of dislocations [25]. At temperatures far below the glass transition temperature, as the mechanical force loaded on a metallic glass exceeds the yield strength, few atoms are first driven by the shear stress to jump. As a result additional defects (i.e. free volume) are introduced, and the regions with higher energy appear. Extension of these regions along the maximum shear stress direction leads to the so-called shear bands. The strain in the shear bands is very high, while that in the areas far from the shear bands is about zero [16]. Correspondingly the microstructure change during the deformation preferentially occurs inside or around the shear bands. For the specimen with high deformation degree, the plastic strain in the alloy at the centers of shear bands is so severe that the deformation-induced disordering surpasses the effect of deformation on the ordering process. Therefore, microstructure evolution is only observed in localized regions near the shear bands.

The above arguments are consistent with the experimental results for $\text{Cu}_{60}\text{Zr}_{20}\text{Ti}_{20}$. Within the investigated plastic strain, the microstructure of the amorphous matrix far from the shear bands is approximately unchanged, indicated by the similar SAED patterns (see Figs. 2a, 6a–d and 7a–d). In contrast, the SAED patterns for the shear bands as shown in Fig. 6a and Fig. 7a are quite different from that of the as-cast state. The first diffraction halos

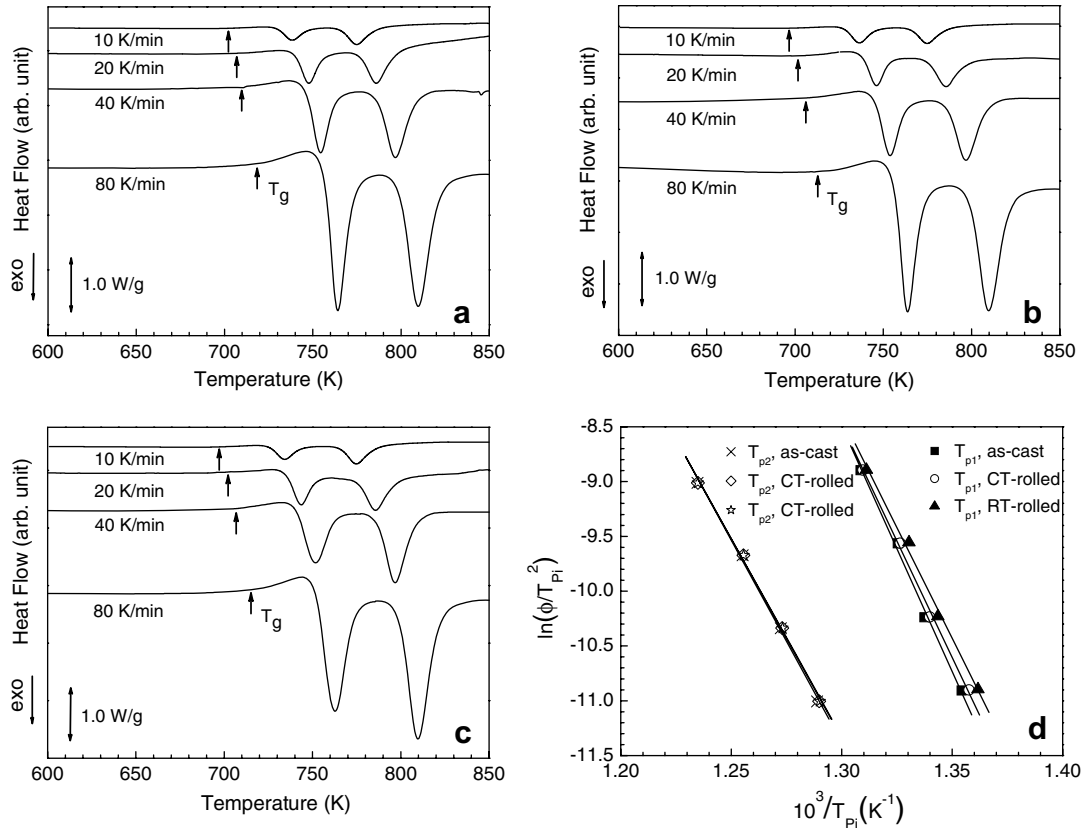


Fig. 9. Isochronal DSC curves of the as-cast specimen (a) and the CT-rolled (b) and RT-rolled (c) specimens with $\varepsilon = 97\%$. (d) The Kissinger plots of $\ln(\phi/T_{pi}^2)$ versus $1/T_{pi}$ for the first ($i = 1$) and second ($i = 2$) exothermic events of the three specimens.

have been considerably broadened, indicating accumulation of free volume in these regions.

In previous work [30], we measured by DSC the free-volume content of $\text{Cu}_{60}\text{Zr}_{20}\text{Ti}_{20}$ metallic glass having undergone different deformation degrees at RT and CT. It was found that the free-volume content during rolling at CT first increases with the deformation degree, and then saturates as the thickness reduction exceeds 89%. When the rolling is performed at RT, although the free-volume content also increases in the earlier stage, it tends to decrease rather than saturate when the thickness reduction exceeds 87%. Since phase separation occurs in the CT-rolled specimens with ε larger than 89%, but partial crystallization in the RT-rolled specimens with ε larger than 87%, it is concluded that the increase of free-volume content in metallic glasses caused by plastic deformation is terminated at the appearance of phase separation or crystallization. As crystallization can absorb some free volume (i.e. enhancing the annihilation rate of free volume), the free-volume content decreases as the crystallization proceeds.

Phase separation is a phenomenon that a homogeneous liquid or amorphous system develops into two or more parts whose compositions are different from each other, while the liquid or amorphous structure is still maintained. When phase separation takes place, from a thermodynamic viewpoint, the free energy of the mixture of the phase-separated regions is lower than that of the original

homogeneous structure. A miscibility gap, which opens up between different thermodynamically favored compositions, induces the occurrence of phase separation [31]. The occurrence of phase separation requires elemental diffusion. For a fully amorphous alloy, it is common to reheat it to temperatures around the glass transition temperature so that the phase separation process can be activated. However, atomic diffusion can also be enhanced by deformation. With the help of shear stress and the increased free volume, a number of atoms are activated during the plastic deformation, promoting the phase separation.

The tendency for phase separation to occur is closely associated with the interatomic action of the alloy. Phase separation might be possible if the heats of mixing among the components differ considerably or, in particular, if there is a positive heat of mixing between two components [32]. A typical system is the well-known $\text{Zr}_{41.2}\text{Ti}_{13.8}\text{Cu}_{12.5}\text{Ni}_{10}\text{Be}_{22.5}$ BMG-forming alloy [33], in which the heats of mixing of Zr–Ti, Zr–Cu, Zr–Ni, Zr–Be, Ti–Cu, Ti–Ni and Ti–Be atomic pairs are 0, –23, –49, –43, –9, –35 and –30 kJ/mol, respectively [34]. The considerable difference in the value of mixing heat leads to the occurrence of phase separation prior to crystallization during the thermal annealing. In another typical phase-separated La–Zr–Al–Cu–Ni metallic glass [35], La and Zr show a positive heat of mixing of 13 kJ/mol, but have negative heat of mixing with the three remaining elements Al, Cu and Ni. While

the alloy melt is rapidly cooled to room temperature, two distinct amorphous phases even directly form in the decomposed melts. For the Cu–Zr–Ti alloy system, the heats of mixing of Cu–Zr, Cu–Ti and Zr–Ti atomic pairs are -23 , -9 and 0 kJ/mol, respectively. Although no positive heat of mixing exists, the large difference in the heats of mixing still makes phase separation possible.

The change of average free-volume content in a metallic glass affects the FWHM measurement result. As the deformation proceeds, the density of shear bands in the $\text{Cu}_{60}\text{Zr}_{20}\text{Ti}_{20}$ glass increases, and the average free-volume content increases, leading to an increasing FWHM. The FWHM is also dependent on the short-range order in metallic glasses. When the $\text{Cu}_{60}\text{Zr}_{20}\text{Ti}_{20}$ specimen is deformed at CT and the thickness reduction has exceeded 89%, it is believed that the short-range order is enhanced as phase separation occurs, verified by the narrowed width of the first diffraction halo from the gray phase-separated region shown in Fig. 6b and d. As a result the FWHM that reflects the structural information of the whole specimen decreases rather than remains fixed. In the RT-rolled $\text{Cu}_{60}\text{Zr}_{20}\text{Ti}_{20}$ specimens, not only phase separation but also nanocrystallization takes place as ε exceeds 87%, leading to a further decrease in the width of the first diffraction halo from the regions of phase separation plus nanocrystallization (compare Figs. 6d and 7d). Correspondingly a large decrease of FWHM is expected.

4.2. Effect of deformation temperature

There are two processes determining the total free-volume content in a deformed metallic glass: annihilation and generation [26]. As the atoms are difficult to activate at lower temperature, the annihilation rate of free volume in the CT rolling is significantly lower than that during the RT rolling, and more free volume is therefore stored in the CT-rolled specimens compared with the RT-rolled specimens when they have the same ε , leading to a higher FWHM (Fig. 4).

The increase of the free-volume content in metallic glasses results in atomic dilatation [36], which enhances atomic mobility and facilitates crystallization. The greater the free-volume content, the more active the atomic mobility. As a result, the specimens undergoing CT rolling would be more prone to crystallization than those undergoing RT rolling, provided that only the influence of free volume is considered. But the fact is that when the specimens were rolled at CT, crystallization was successfully suppressed due to the lower deformation temperature, and only phase separation occurred at the higher ε , while nanocrystals appeared in the RT-rolled specimens at a lower ε even though their free-volume content was lower. For the CT rolling, the enhanced atomic mobility resulting from the increasing free-volume content fails to compensate the reduced atomic mobility from the lower temperature. As such, lowering the deformation temperature is an effective way of carefully investigating the microstructural evolution

of metallic glasses with deformation. Our results clearly indicate that as the deformation proceeds, the $\text{Cu}_{60}\text{Zr}_{20}\text{Ti}_{20}$ metallic glass is first separated into different composition regions, and then crystallization occurs in them. Raising the deformation temperature shortens the interval between the onset times of phase separation and crystallization, and finally these two processes take place simultaneously, just as has been observed in RT rolling.

4.3. Stability of the deformed glass against heating

The deformation with low ε mainly causes the free-volume content in the $\text{Cu}_{60}\text{Zr}_{20}\text{Ti}_{20}$ metallic glass to increase. Both the onset temperature and enthalpy for the first crystallization event do not change with the deformation when ε is not too high (Fig. 5c and d). The effective activation energy derived from the Kissinger plots, which is determined by nucleation and growth of crystal in the metallic glass, remains invariable.

If the deformation degree achieved in the experimental material is enough high, i.e. larger than 87% for RT rolling and 89% for CT rolling, a large proportion of atoms inside the regions with high free-volume content are activated by the shear stress and can cause long-range diffusion. Thus the topological short-range order in the metallic glass is enhanced, and phase separation is created so as to decrease the free energy of the system until crystals with the lowest free energy form.

The phase separation at high ε produces many regions whose compositions have changed compared to that of the original amorphous phase. Nucleation and growth of the primary phase in such regions requires less solute diffusion and therefore takes place at lower temperature during the annealing treatment and exhibits decreased activation energy. Especially in the RT-rolled specimens, the composition of the phase-separated regions is much closer to that of the primary phase due to the relatively high atomic mobility, and some of the regions even contain nanocrystals. These crystals can act as nucleation sites during the subsequent annealing, and grow without considerable solute diffusion. Hence, such deformed specimens have a further degraded thermal stability.

5. Conclusions

By carefully controlling the strain rate, a thickness reduction as high as 97% has been achieved in the rolling of $\text{Cu}_{60}\text{Zr}_{20}\text{Ti}_{20}$ BMG at two different temperatures, CT and RT. Investigation of the microstructure leads to the following conclusions for this material:

- (1) During the plastic deformation at temperatures far below the glass transition temperature, the material inside or near the shear bands undergoes a severer deformation compared with the region far away from the shear bands, so the deformation-induced structural evolution preferentially occurs in it.

- (2) Corresponding to each deformation temperature, there is a critical deformation degree for the alloy. It is 89% at CT and 87% at RT. Below the critical deformation degree, plastic deformation merely creates shear bands in the glass. When the deformation degree exceeds the critical value, substructures with composition different from the nominal composition of the alloy precipitate in the amorphous matrix. Their deviation in average composition from that of the amorphous matrix is enhanced as the deformation temperature is increased from CT to RT. The substructures in the RT-rolled specimens consist of phase-separated regions and nanocrystals, while those in the CT-rolled specimens are fully amorphous.
- (3) The thermal stability of the glass against crystallization does not change with deformation below the critical deformation degree. As the deformation degree exceeds the critical value, however, the thermal stability is decreased owing to the phase separation. If the deformation leads to nanocrystallization, just as occurs in the RT rolling, the thermal stability will be further reduced.

Acknowledgements

The authors thank H. Rasmussen, F. Xu and J. Saida for help in preparing the specimens and the HRTEM observations. Financial support from the National Natural Science Foundation of China (Grant No. 50471016) and the DANIDA Fellowship Center is gratefully acknowledged. Financial support for J.Z.J. from the National Natural Science Foundation of China (Grant Nos. 50341032 and 50425102), the Ministry of Science and Technology of China (Grant Nos. 2004/249/37-14 and 2004/250/31-01 A), the Ministry of Education of China (Grant Nos. 2.005E+10 and 2005-55) and Zhejiang University is gratefully acknowledged.

References

- [1] Inoue A. *Acta Mater* 2000;48:279.
- [2] Johnson WL. *MRS Bull* 1999;24:42.
- [3] Greer AL. *Science* 1995;267:1947.
- [4] Leamy HJ, Chen HS, Wang TT. *Metall Trans* 1972;3:699.
- [5] Zhang ZF, Eckert J, Schultz L. *Acta Mater* 2003;51:1167.
- [6] Mukai T, Nieh TG, Kawamura Y, Inoue A, Higashi K. *Scripta Mater* 2002;46:43.
- [7] Gilbert CJ, Ritchie RO, Johnson WL. *Appl Phys Lett* 1997;17:476.
- [8] Xi XK, Zhao DQ, Pan MX, Wang WH, Wu Y, Lewandowski JJ. *Phys Rev Lett* 2005;94:125510.
- [9] Pampillo CA. *J Mater Sci* 1975;10:1194.
- [10] Gao MC, Hackenberg RE, Shiflet GJ. *Mater Trans* 2001;42:1741.
- [11] Liu CT, Heatherly L, Easton DS, Carmichael CA, Schneibel JH, Chen HC, Wright JL, Yoo MH, Horton JA, Inoue A. *Metall Mater Trans A* 1998;29:1811.
- [12] Bruck HA, Rosakis AJ, Johnson WL. *J Mater Res* 1996;11:503.
- [13] Jiang WH, Pinkerton FE, Atzmon M. *Scripta Mater* 2003;48:1195.
- [14] Kim JJ, Choi Y, Suresh S, Argon AS. *Science* 2002;295:654.
- [15] Jiang WH, Pinkerton FE, Atzmon M. *J Appl Phys* 2003;93:9287.
- [16] Chen H, He Y, Shiflet GJ, Poon SJ. *Nature* 1994;367:541.
- [17] Jiang WH, Atzmon M. *Appl Phys Lett* 2005;86:151916.
- [18] Saida J, Setyawan ADH, Kato H, Inoue A. *Appl Phys Lett* 2005;87:151907.
- [19] Das J, Tang MB, Kim KB, Theissmann R, Baier F, Wang WH, Eckert J. *Phys Rev Lett* 2005;94:205501.
- [20] Cao QP, Li JF, Zhou YH, Jiang JZ. *Appl Phys Lett* 2005;86:081913.
- [21] Chang HJ, Park ES, Kim YC, Kim DH. *Mater Sci Eng A* 2005;406:119.
- [22] Jiang JZ, Kato H, Ohsuna T, Saida J, Inoue A, Saksl K, Franz H, Ståhl K. *Appl Phys Lett* 2003;83:3299.
- [23] Concustell A, Révész Á, Suriñach S, Baró MD, Varga LK, Heunen G. *J Mater Res* 2004;19:505.
- [24] Jiang JZ, Yang B, Saksl K, Franz H, Pryds N. *J Mater Res* 2003;18:895.
- [25] Spaepen F. *Acta Metall* 1977;25:407.
- [26] Huang R, Suo Z, Prevost JH, Nix WD. *J Mech Phys Solids* 2002;50:1011.
- [27] Steif PS, Spaepen F, Hutchinson JW. *Acta Metall* 1982;30:447.
- [28] Zhuang YX, Wang WH. *J Appl Phys* 2000;87:8209.
- [29] Kissinger HE. *J Res Natl Bur Stand* 1956;57:217.
- [30] Cao QP, Li JF, Zhou YH, Horesewell A, Jiang JZ. *Appl Phys Lett* 2005;87:101901.
- [31] Busch R, Schneider S, Peker A, Johnson WL. *Appl Phys Lett* 1995;67:1544.
- [32] Park BJ, Chang HJ, Kim DH, Kim WT. *Appl Phys Lett* 2004;85:6353.
- [33] Schneider S, Thiyagarajan P, Johnson WL. *Appl Phys Lett* 1996;68:493.
- [34] Takeuchi A, Inoue A. *Mater Trans JIM* 2000;41:1372.
- [35] Kundig AA, Ohnuma M, Ping DH, Ohkubo T, Hono K. *Acta Mater* 2004;52:2441.
- [36] Donovan PE, Stobbs WM. *Acta Metall* 1981;29:1419.